

# A Zero-Threshold Polariton-Raman Laser

Avijit Dhara<sup>1†</sup>, Devarshi Chakrabarty<sup>1†</sup>, Pritam Das<sup>1†</sup>, Kritika Ghosh<sup>2</sup>, Ayan Roy Chaudhuri<sup>2</sup>, Sajal Dhara<sup>1\*</sup>

<sup>1</sup>*Department of Physics, IIT Kharagpur, Kharagpur-721302, India*

<sup>2</sup>*Materials Science Centre, IIT Kharagpur, Kharagpur-721302, India*

<sup>†</sup> *These authors contributed equally*

<sup>\*</sup> *Corresponding author. email: sajaladhara@phy.iitkgp.ac.in*

## Abstract:

Raman lasers are known for their low power operation and wavelength tunability unattainable by conventional lasers<sup>1-5</sup>. Recently ultralow-threshold Raman lasers had been realized in semiconductors with various geometries<sup>6-8</sup>. Zero-threshold lasers were realized previously only in single atom emitter strongly coupled in a single mode cavity<sup>9-13</sup> with spontaneous emission coupling factor of unity. However, this was not feasible in microcavities hosting isotropic Raman active materials with degenerate bare cavity modes<sup>14,15</sup>. Here we show that a zero threshold Raman laser can be achieved when Stoke shifted polariton Raman modes are tuned within one of the anisotropic exciton-polariton bands in an optical microcavity. In addition, we demonstrate that Raman active anisotropic exciton-polaritons in a single mode microcavity offers a platform to realize a PT-symmetric non-Hermitian quantum system of two nearly orthogonal polariton modes that constitute a non-trivial band dispersion containing exceptional points. We found that the PT-symmetric phase responsible for the zero-threshold lasing can be switched to a finite threshold in PT-symmetry broken phase via cavity detuning by the variation of bath temperature, as well as by the variation of pump polarization and energy. Our discovery of zero threshold polariton Raman laser, would not only open up several new paradigms of applications in the areas of quantum optics and on-chip photonics but also offer a platform for research in quantum physics of PT-symmetric non-Hermitian system.

## Introduction:

Significance of threshold less lasers lies not only in their low footprint and low noise features, but also in their non-classical character. A threshold-less laser in a solid state system, therefore, could be a quantum leap in the frontier of micro-lasers in the broad area of applications in quantum optics and on-chip photonics. However, high values of spontaneous emission coupling factor ( $\beta$ )<sup>16-18</sup> has been reported earlier but none could achieve the absolute value of unity required for a zero threshold laser.

In this work, we demonstrate zero threshold polariton Raman laser with  $\beta$  value of unity involving normal modes of anisotropic exciton-polaritons, by pumping at a higher energy polariton branch while the Stokes shifted polariton Raman (PR) mode is supported by a lower energy polariton branch. An anisotropic 2D semiconductor has been utilized as the Raman active material embedded in a planar microcavity that supports two non-degenerate cavity modes, along with two highly polarized excitons, resulting in two sets of exciton-polariton bands with two different polarizations. For a particular polarization of the probe beam, this system enables us to project a specific section of polariton dispersion in two-dimensional parameter space of polarization and in-plane momentum. Such open quantum systems are being understood recently using non-Hermitian description<sup>19-31</sup>. Prior to this work we established the existence of non-trivial exciton-polariton bands (manuscript to appear soon)

with exceptional points (EPs) where the system can be excited to observe the intriguing physics of zero threshold PT-symmetric Raman lasing that we present in this article. If excited at one of the EPs, two Stoke shifted PR states are also degenerate with two different polarizations. The key criterion for PT-symmetry is satisfied easily when one of the polarization states of the PRs lies in the lower polariton band with identical polarization (thus providing the gain), whereas, the other polarization state of the PR mode appears at the stop band of the polariton dispersion (as shown in Fig. 1b) and hence introducing a loss. Note that the realization of the classical PT-symmetry in optics that has been achieved so far<sup>32–37</sup> is from the analogy of Schrodinger equation which, with certain approximation, resembles the equation of electromagnetic wave propagation in a medium<sup>38,39</sup>. In contrast, the exciton-polariton PT-symmetry that has been realized in this work is truly in the quantum regime and hence can lead to a different physics additionally governed by quantum noise<sup>40</sup>. Therefore, strong Raman active modes in ReS<sub>2</sub> embedded optical microcavity provides an interesting platform to explore PT-symmetric non-Hermitian physics of light-matter interactions in the domain of cavity quantum electrodynamics. Stimulated Raman scattering, observed for every Stokes line lying within the range of the polariton bands thus offers a promising platform to realize PT-symmetric exciton-polariton-Raman laser. We demonstrate that some of these stimulated Raman lines are zero threshold polariton Raman laser (ZTPRL) when the excitation energy is in the vicinity of an EP of the polariton dispersion and otherwise show a finite threshold if the polariton branch is detuned. Zero to finite threshold transitions are related to PT-symmetric phase to PT-Symmetry broken phase which can also be observed by detuning the cavity modes as well as introducing more loss by increasing the bath temperature.

2D transition metal dichalcogenides (TMDs), with their novel excitonic properties<sup>41</sup>, are being recognized as a potential active laser medium<sup>42,43</sup> and an ideal platform for realising exciton-polaritons via strong light-matter coupling<sup>44,45</sup>. ReS<sub>2</sub> is a member of 2D TMDs, known for its distorted 1T crystal structure hosting strongly polarized excitons<sup>46,47</sup>, and its ability to realize strong light-matter coupling<sup>48</sup>. Due to its low symmetry, it has 18 Raman modes in the range of 100 to 450  $cm^{-1}$ <sup>49</sup>. One of the interesting properties of bare ReS<sub>2</sub> is the quenching of the photoluminescence intensity at near resonant excitation and emergence of Raman peaks dominating the emission spectrum<sup>50</sup>. Thus, ReS<sub>2</sub> offers a unique platform for observing Raman lasing. A 10 nm layer of mechanically exfoliated single crystalline ReS<sub>2</sub> was sandwiched inside optical microcavity in this experiment to observe the Raman lasing (see methods) as shown in the schematic of Fig. 1a.

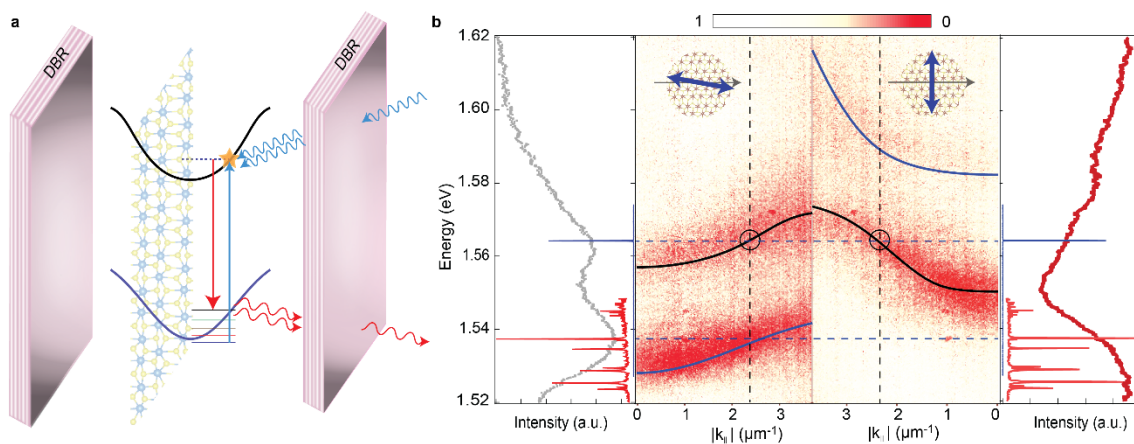


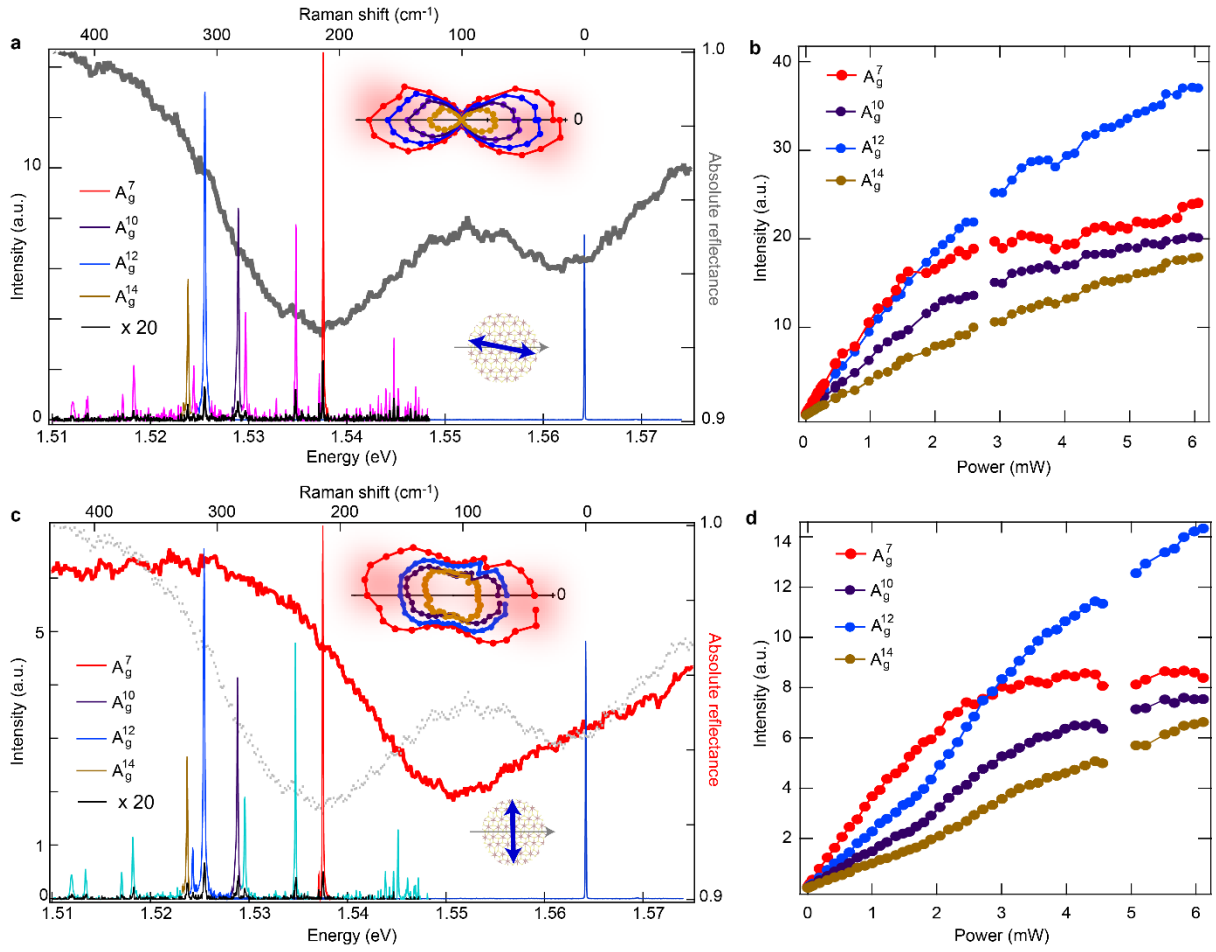
**Figure 1: Schematic of the optical microcavity along with experimental data rendering the mechanism of zero threshold polariton Raman laser:** (a) Schematic of the single mode optical microcavity comprising of an ReS<sub>2</sub> crystal embedded within two distributed Bragg reflectors (DBR). The stimulated Raman scattering mechanism is shown when the sample is excited in the upper polariton branch (blue arrow), and the emission from

the Stokes shifted PR mode from the lower polariton branch (red arrow). (b) Left and right panels are experimentally observed angle-resolved reflectance showing polariton dispersions probed by linearly polarized light along  $d_1$  and  $d_2$  respectively. The exceptional points at the same energy ( $\sim 1.564$  eV) and momentum in the polariton bands are marked by a black circle. Panels at extreme left and right showing the spectrum of the pump beam (blue peak with intensity in arbitrary scale) and the Stokes shifted stimulated emissions from PR modes overlaid with the integrated reflectance at two different pump polarizations ( $d_1$  and  $d_2$ ) as shown in the inset.

The biaxiality of ReS<sub>2</sub> splits the transverse electric (TE) and transverse magnetic (TM) cavity modes, which interact with two anisotropic excitons ( $X_1$  and  $X_2$ ) to form four polariton normal modes which we denote as  $X_1$  upper ( $U_1$ ),  $X_1$  lower ( $L_1$ ),  $X_2$  upper ( $U_2$ ) and  $X_2$  lower ( $L_2$ ) polariton branches. Light-matter interactions in this anisotropic material and the polariton dispersions can be understood by diagonalizing the following Hamiltonian:  $H = \hbar\omega_i C_i^\dagger C_i + \hbar\omega_j X_j^\dagger X_j + v_j \hat{e}_i \cdot \hat{d}_j [C_i^\dagger X_j + X_j^\dagger C_i]$ . Here,  $C_i$ ,  $X_j$  are the annihilation operators for the photonic and excitonic modes respectively,  $\hat{e}_i$  is the in-plane polarization unit vector of the photonic modes. Indices  $i$  and  $j$  labels the TE, TM, and two anisotropic excitons  $X_1$ ,  $X_2$  respectively. We define the anisotropic axes  $d_1$  and  $d_2$  by observing the absorption maxima with respect to the polarization directions along  $X_1$  and  $X_2$  respectively. These two axes are not exactly orthogonal and make an angle of 170 ( $d_1$ ) and 90 ( $d_2$ ) degrees with the crystallographic b-axis respectively, resulting in finite coupling between the  $X_1$  ( $U_1$ ,  $L_1$ ) and  $X_2$  ( $U_2$ ,  $L_2$ ) polariton band sectors. Two sections of polariton dispersions for two special polarizations of the probe beam are shown in the angle resolved reflectivity data in Fig. 1b. In the left extreme (Fig. 1b) we show the energy position of the pump beam, polarized along the  $d_1$  axis at the exceptional point and corresponding Stokes lines lie within  $L_1$  band vertically below the point of excitation, hence, providing amplification or gain. In the extreme right (Fig. 1b) we show the pump beam, polarized along the  $d_2$  axis at the exceptional point and corresponding stokes lines are lossy as they fall in the stop band of the cavity. However, due to non-orthogonality of  $d_1$  and  $d_2$ , both the polariton modes ( $U_1$  and  $L_2$ ) are being excited at the exceptional point with amplitudes depending on the polarization components. The degenerate polariton modes with two different polarizations generate the stokes shifted PR which we describe with a non-Hermitian PT-symmetric mechanism in subsequent sections.

Irrespective of pump polarization, we identify several Raman modes from existing literature for ReS<sub>2</sub> with AA stacking order (Method and Extended Data Fig. 1). Out of these Raman peaks we focus on four lines labeled by different colours:  $A_g^7$  ( $214\text{ cm}^{-1}$ ),  $A_g^{10}$  ( $284\text{ cm}^{-1}$ ),  $A_g^{12}$  ( $311\text{ cm}^{-1}$ ) and  $A_g^{14}$  ( $325\text{ cm}^{-1}$ ) as shown in fig 2a and 2c<sup>49</sup>. In Fig. 2a, we show the stimulated Stokes emissions when we pump at the EP with 792.6 nm wavelength (as shown in Fig. 1b left panel) and polarization along  $d_1$ . The Stoke shifted PR lines lie within the  $L_1$  band and we observe  $\sim 150$  to 300 times enhancement in the emission intensity compared to bare ReS<sub>2</sub> of similar thickness on the SiO<sub>2</sub>/Si substrate. Note that the  $L_2$  band is also being excited due to non-orthogonality of  $d_1$  and  $d_2$ , however, the corresponding PR modes are not supported by any polariton modes below, and hence they are attenuated. Therefore, the PT-symmetry reinforces only one PR mode in the system. Top inset of Fig. 2a shows the emission is highly polarized along  $d_1$  axis, same as the polarization state of  $L_1$  and  $U_1$ . In this case, the spontaneous coupling factor ( $\beta$ ) is unity, and the Raman gain profiles for each of the PR modes at different energies independently overlap with only one polariton mode  $L_1$ . Linear power dependence (down to 180 nW, Extended Data Fig. 2) of the Raman intensity reveals the signature of the zero-threshold lasing which gets finally saturated at higher power for some of the Raman lines as shown in Fig 2b, a trend previously observed in single trapped atom laser from microcavity<sup>11</sup>. A rate equation model has been discussed (see Methods) to understand this linear power dependence which is expected in ZTPRL. The spectral linewidths ( $\sim 0.5\text{ \AA}$ ) of these Raman peaks are very narrow, falling

within our spectrometer resolution. Same set of Raman peaks are observed when the polarization is



switched to along  $d_2$  as shown in Fig. 2b. However, only one PR mode ( $A_g^7$ ) shows ZTPRL and this turns out to be robust for all polarizations of the pump beam. We observe considerable changes not only in the intensity polar plot of emitted lines, but also in the power dependence.

**Figure 2: Observation of polariton Raman lasing with signature power dependence for zero and finite threshold lasers at two different polarizations of pump beam:** (a) Showing emission spectra of various polariton Raman modes when excited at a pump energy 1.564 eV (blue peak at extreme right) along  $d_1$  polarization. The spectrum is overlaid with the integrated reflectance (grey color) at this particular polarization of probe beam. Distinct PR modes  $A_g^7$ ,  $A_g^{10}$ ,  $A_g^{12}$  and  $A_g^{14}$ , are labelled with different colours. The Raman spectra from bare ReS<sub>2</sub> on SiO<sub>2</sub> (black spectrum, multiplied by 20X) is shown in the same plot for comparison. The polarization dependence of intensity variation with analyzer angle in reference to the b-axis is shown in the inset in a polar plot of four PR modes. (b) Power dependence of intensity of polariton Raman modes showing the zero threshold characteristics for all four PR modes when the pump polarization is along  $d_1$ . (c) Same as (a) with pump polarization along  $d_2$ . (d) Power dependence of intensity of polariton Raman modes showing the finite threshold lasing behavior with a threshold power around 2 mW for  $A_g^{10}$ ,  $A_g^{12}$  and  $A_g^{14}$  with pump polarization is switched along  $d_2$ . The  $A_g^7$  mode is the most dominant lasing mode having robust zero-threshold characteristics in both the polarizations of the pump beam.

Components of polarizations of the PR modes are still maximum along  $d_1$  with non-zero  $d_2$  components for all the modes. Interestingly, the power dependence now shows finite threshold with familiar S-shaped non-linearity particularly for the PR peaks of  $A_g^{10}$ ,  $A_g^{12}$  and  $A_g^{14}$  with a threshold

power of  $\sim 2$  mW. Despite stronger excitation in the  $L_2$  band it results in a lossy PR mode responsible for weaker emission of polarized component along  $d_2$ . We observed usual linear power dependence of spontaneous Raman emission of this polarized component (Extended Data Fig. 3). The interplay between loss, gain, and their interactions between two PR modes leading to ZTPRL is controlled by the polarization, and energy of the pump beam where the PT-symmetric system undergoes transition from a PT – symmetric phase (zero-threshold) to a PT – broken phase (finite threshold) as discussed below.

Each point in the polariton band as shown in Fig. 1b represents an energy eigenstate of a polariton mode for a particular in-plane momentum and polarization. We consider two Stoke shifted degenerate states  $|\psi_1(\epsilon, k_{EP})\rangle$ , and  $|\psi_2(\epsilon, k_{EP})\rangle$  vertically below the EP of bands  $U_1$  and  $L_2$  having energies  $\epsilon + i\delta_1$ ,  $\epsilon - i\delta_2$  respectively. The sign of the imaginary part in energies are inferred from the observations of gain or loss, where,  $\delta_1$  and  $\delta_2$  are positive. These states are having finite overlap or coupling ( $g$ ) due to slight non-orthogonality as discussed earlier. Hamiltonian in this subspace of twofold degenerate states can be written in non-Hermitian form:

$$H = (|\psi_1\rangle, |\psi_2\rangle) \begin{pmatrix} \epsilon + i\delta_1 & g \\ g & \epsilon - i\delta_2 \end{pmatrix} \begin{pmatrix} \langle \psi_1 | \\ \langle \psi_2 | \end{pmatrix} \dots\dots\dots (1)$$

In the case of finite threshold lasing, we observe one lasing mode and one non-lasing mode at the same energy ( $\epsilon = 1.537$  eV). This is only satisfied in the coupling regime,  $g \leq \delta$ , where,  $\delta = \frac{(\delta_1 + \delta_2)}{2}$ , together with the condition,  $\delta_1 = \delta_2$  (discussed in methods). This is so called the PT-broken phase of a non-Hermitian PT-symmetric Hamiltonian responsible for finite threshold lasing with the diagonal elements being complex conjugate. The value of  $\delta_1$ , and  $\delta_2$  can be estimated from the Purcell factor ( $F \sim 40$ ) and the linewidth ( $\gamma \sim 10$  meV) of the  $L_1$  polariton mode using the relation:  $\delta_2 = \delta_1 = \delta = \frac{\gamma}{2} \ln(F) \sim 18$  meV. For, excitation polarization along  $d_2$ , a large amplitude of  $|\psi_2\rangle$  is attenuated as it falls in the stop band of the cavity, satisfying the condition  $g < \delta$ , responsible for the finite threshold lasing in PT symmetry broken phase.

On the other hand, ZTPRL is obtained when only a single mode exists inside the cavity, or when the eigenmodes coalesce. This happens in the case when  $g \rightarrow \delta$ . In this condition, the eigenvalues are real and degenerate, and the system is in PT-symmetric phase. Our experimental observations suggest that the overlap coupling factor  $g$  should depend on the pump polarization, which can be understood as follows: When excitation is  $d_1$  polarized, a large amplitude of  $|\psi_1\rangle$  being amplified as it is supported by  $L_1$  causing the enhancement in  $g$  to its maximum  $g = \delta$ , which is responsible for the zero-threshold lasing action. Interestingly, we observe only the  $A_g^7$  mode which coincides exactly at the dip of the  $L_1$  band shows ZTPRL irrespective of the polarization of the pump beam (as seen in Fig. 2). Note that unlike other PT-symmetric lasers<sup>32,33</sup>, the interplay of loss and gain in this system is associated with the polarized polaritons, resulting in linearly polarized lasing mode supported by the cavity.

From the above discussion, it is expected that if the polariton modes are detuned while keeping the excitation energy fixed,  $g$  should change and allow us to observe the zero to finite threshold transition in the power dependence of the emission intensity. This is verified by varying the bath temperature of the system. As temperature increases, a redshift of the polariton modes and an increase in their linewidths changes the reflectance dip in  $\text{ReS}_2$ <sup>47</sup>. This enables us to detune the PR modes  $|\psi_1\rangle$  and  $|\psi_2\rangle$  with respect to the  $L_1$ , and  $U_2$  bands that can influence  $g$  and  $\delta$ . As temperature increases, a redshift of the polariton modes and an increase in their linewidths changes the reflectance dip in

$\text{ReS}_2^{47}$ . This enables us to detune the PR modes  $|\psi_1\rangle$ , and  $|\psi_2\rangle$  with respect to the  $L_1$ , and  $U_2$  bands that can influence  $g$  and  $\delta$ .

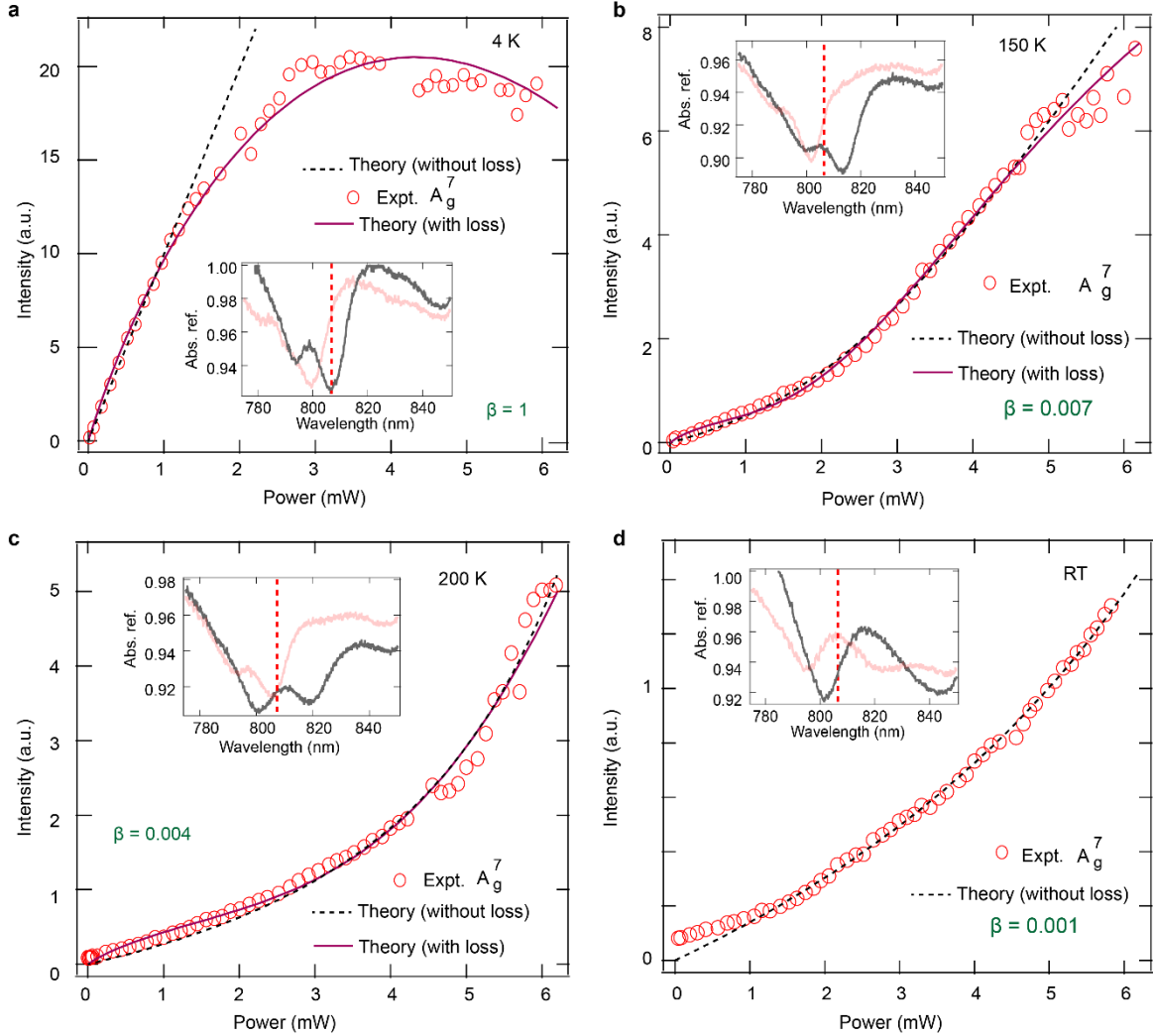


**Figure 3: Zero to finite threshold transition of polariton Raman laser ( $A_g^7$  mode) via cavity detuning and loss at higher temperatures:** Power dependence of intensity of the lasing mode when polarization is fixed along  $d_2$ . The empty circles represent experimental data, solid (dashed) lines are theoretical curves as obtained from the rate equation model with (without) nonlinear loss as given in the main text (Eq. 2). (a) at 4 K, the power dependence data agrees best with  $\beta = 1$ . (b) At 150 K, finite threshold is observed with a pre-threshold linear region preceding a kink at 2.3 mW with  $\beta = 0.007$ . (c) At 200 K, finite threshold persists with a higher threshold pump power of 4.5 mW with  $\beta = 0.004$ , and (d) At room temperature, lasing threshold is not reached with  $\beta = 0.001$ . In each inset, the peak position of  $A_g^7$  mode has been shown (red dashed line) with respect to polariton mode absorption dips (grey and red for  $X_1$  and  $X_2$  polariton modes respectively) for different temperatures.

In Fig. 3a-d we show the temperature evolution of the power dependence for the  $A_g^7$  mode which shows robust ZTPRL at 4 K, for polarization of the pump beam along  $d_2$ . At 150 K (Fig.3b), the polariton branch is redshifted with a broader linewidth (shown in the inset of fig 3b). A prominent non-linear power dependence is observed with a finite threshold power of 2.3 mW, as shown in Fig. 3b, indicating transition to a PT-symmetric to PT-broken phase due to change in  $g$  and  $\delta$ . Further reduction in  $g$  and increment in  $\delta$  via detuning and loss is observed at 200 K, resulting in a threshold power of 4.5 mW. Finally, at room temperature as shown in Fig. 3d, completely detuned from the  $A_g^7$  mode, showing no

trace of Rabi splitting since the exciton oscillator strength is too low for strong coupling. At this temperature, the system evidently cannot reach the threshold condition within the range of power variation. Therefore, the temperature variation of laser threshold can be interpreted with the non-Hermitian PT-symmetric description as presented above.

Finally, to understand the power dependence in this system we propose a rate equation model (see Methods), relating the PR intensity ( $I_{out}$ ) with the pump power ( $P_{int}$ ) as follows:

$$I_{out} \propto \frac{1}{2} \left( P_{int} + \beta - 1 - \beta F + \sqrt{(\beta - 1 - P_{int} + \beta F)^2 + 4\beta F P_{int}} \right) \dots\dots\dots (2)$$

Where the spontaneous emission coupling factor  $\beta \leq 1$ , the equality holds when a single mode is present in the cavity, which happens only in the PT-symmetric phase. The Purcell factor F can be estimated for our microcavity to be  $\sim 40$ , which has been used in the model to fit the observed power dependence. In case of zero threshold lasing (in the PT-symmetric condition) where  $\beta = 1$ , the power dependence is linear as shown using dashed lines in Fig.3a and Fig. 4a. The observed saturation at higher power can be attributed to 3<sup>rd</sup> order non-linear processes whose effect can be captured by including one loss term ( $\propto P_{int}^{1.5}$ ) in the above relation, as shown by the solid lines in Fig. 3a-c and 4. For more than one mode ( $\beta < 1$ ),  $I_{out}$  vs  $P_{int}$  is a nonlinear S-shaped curve, which is characteristic of finite threshold lasing.

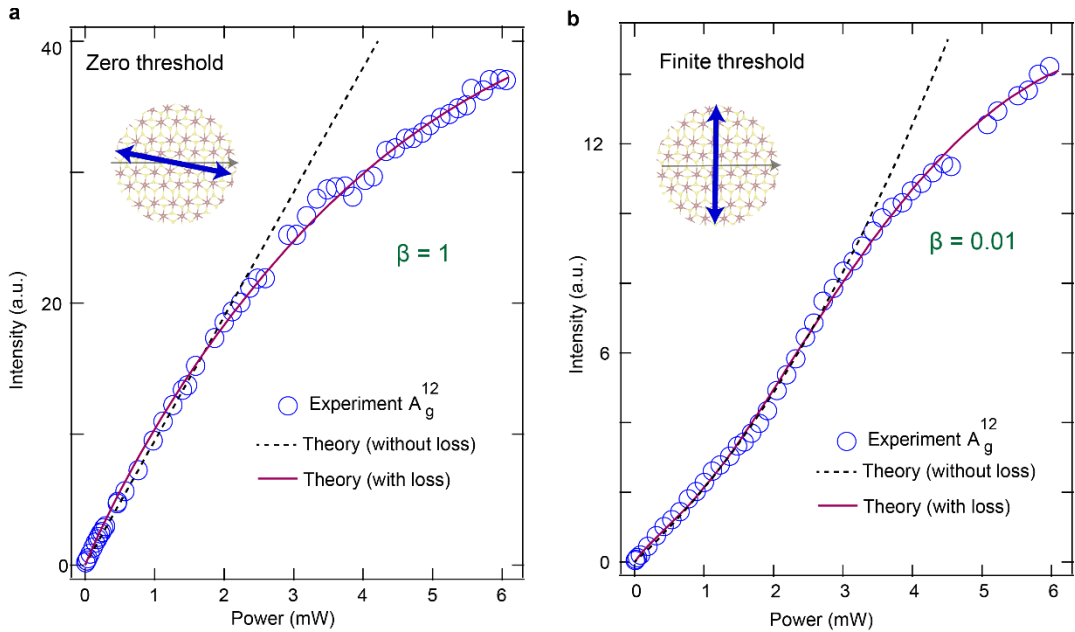


**Figure 4: Zero to finite threshold transition of polariton Raman laser via polarization of pump beam:** Power dependence of the  $A_g^{12}$  lasing mode at two different pump polarizations. The empty circles represent experimental data, solid (dashed) lines are theoretical curves as obtained from the rate equation model with (without) nonlinear loss as given in the main text (Eq. 2). (a) Pump polarization along  $d_1$  when the power dependence data agrees best with  $\beta = 1$ . (b) Pump polarization is switched along  $d_2$  with the power dependence data showing finite threshold power of 1.9 mW which agrees well with  $\beta = 0.01$ .

Switching between the PT-symmetric ( $\beta = 1$ ) to PT-broken phase ( $\beta \leq 1$ ), controlled by the polarization of the pump beam, shows up with distinct power dependence of  $A_g^{12}$  mode that can be modeled with  $\beta = 1$  for  $d_1$  polarized excitation which changes to  $\beta = 0.01$  for  $d_2$  polarized excitation as shown in Fig. 4a. The variation of  $\beta$  as a function of temperature giving rise to the transition

between ZTPRL to finite threshold lasing as discussed above, can be observed in Fig. 3a-c at three different temperatures. Here  $\beta$  varies from unity at 4 K to 0.004 at 200 K.

All the lasing modes that have been discussed above has directionalities around different angle of emissions satisfying momentum matching conditions as shown in the angle resolved measurement in the extended data 7. However, no directionality has been observed for any of the non-lasing modes irrespective of enhancement of Raman intensities. The robustness of zero threshold lasing and all the experimental results as discussed above has been observed in a different ReS<sub>2</sub> flake of similar thickness inside the same cavity, rotated and brought to the same orientation as the previous one, which is shown in the extended data 8. Note that the polariton dispersions, occurrence of EP, and the realization of PT-symmetry as presented in Fig. 1b, depends on the angular orientation of the sample which has been discussed in detail in our recent work (manuscript to appear soon). A different orientation of the same sample thus allows us to excite the system at the same energy of the pump beam where there is no EP as shown in the extended data 9. In this orientation which we obtain by rotating the sample by 45 degrees, a robust ZTPRL has been observed for all the PR modes when the pump polarization is along  $d_1$ , however, as expected, no lasing modes has been observed when the pump polarization is along  $d_2$  as shown in the extended data. Therefore, in the absence of EP, ZTPRL can be observed only at a specific polariton branch ( $L_1$ ), where the PT-symmetry protection is not required as only a single PR mode being is excited.

In conclusion, we demonstrated zero threshold polariton Raman laser from a system of anisotropic microcavity exciton-polaritons. To the best of our knowledge this work first time highlights the significance of exceptional point in an open quantum system of exciton-polaritons for the realization of zero threshold lasers in a solid-state system. This work demonstrates that non-degenerate cavity modes due to microscopic anisotropy of the Raman active medium is an essential ingredient to achieve the PT-symmetry ensuring the  $\beta$  factor value of unity for the single mode lasing. We expect that the threshold less lasing action demonstrated in our system is quite generic and could be observed in any single mode microcavity hosting anisotropic Raman active materials supporting polarized excitons. We believe our work not only paves the way towards a new frontier of tunable, zero threshold micro lasers for applications in quantum optics but it also offers a system for fundamental research in quantum physics of non-Hermitian PT-symmetry and topological polaritons.

#### **Acknowledgements:**

This work has been supported by funding from the Science and Engineering Research Board (CRG/2018/002845, CRG/2021/000811); Ministry of Education (MoE/STARS- 1/647); Council of Scientific and Industrial Research, India (09/081(1352)/2019-EMR-I); Department of Science and Technology, Ministry of Science and Technology, India (IF180046) and Indian Institute of Technology Kharagpur. We thank Prof. Sugata Pratik Khastgir for valuable discussions with him during this work.

#### **Author contributions:**

SD conceptualized the project. AD, DC, KG, ARC and SD contributed in the sample fabrication. AD, DC, PD and SD formulated the experiments, performed data analysis, and developed the theory. AD, DC, PD performed all optical measurements. AD, DC, PD and SD drafted the paper, and all authors contributed to reviewing and editing the final draft. SD supervised the project.

## References:

1. Nishizawa, J. & Suto, K. Semiconductor Raman laser. *Journal of Applied Physics* **51**, 2429–2431 (1980).
2. Rong, H. *et al.* An all-silicon Raman laser. *Nature* **433**, 292–294 (2005).
3. Rong, H. *et al.* A continuous-wave Raman silicon laser. *Nature* **433**, 725–728 (2005).
4. Latawiec, P. *et al.* On-chip diamond Raman laser. *Optica* **2**, 924 (2015).
5. Cao, Q.-T. *et al.* Reconfigurable symmetry-broken laser in a symmetric microcavity. *Nat Commun* **11**, 1136 (2020).
6. Spillane, S. M., Kippenberg, T. J. & Vahala, K. J. Ultralow-threshold Raman laser using a spherical dielectric microcavity. *Nature* **415**, 621–623 (2002).
7. Grudinin, I. S. & Maleki, L. Ultralow-threshold Raman lasing with CaF<sub>2</sub> resonators. *Opt. Lett., OL* **32**, 166–168 (2007).
8. Takahashi, Y. *et al.* A micrometre-scale Raman silicon laser with a microwatt threshold. *Nature* **498**, 470–474 (2013).
9. De Martini, F. & Jacobovitz, G. R. Anomalous spontaneous--stimulated-decay phase transition and zero-threshold laser action in a microscopic cavity. *Phys. Rev. Lett.* **60**, 1711–1714 (1988).
10. Mu, Y. & Savage, C. M. One-atom lasers. *Phys. Rev. A* **46**, 5944–5954 (1992).
11. McKeever, J., Boca, A., Boozer, A. D., Buck, J. R. & Kimble, H. J. Experimental realization of a one-atom laser in the regime of strong coupling. *Nature* **425**, 268–271 (2003).
12. Astafiev, O. *et al.* Single artificial-atom lasing. *Nature* **449**, 588–590 (2007).
13. Dey, A., Pal, A., Gupta, S. D. & Deb, B. Zero-threshold correlated-photon laser with a single trapped atom in a bimodal cavity. Preprint at <http://arxiv.org/abs/2207.12304> (2022).
14. Fainstein, A., Jusserand, B. & Thierry-Mieg, V. Raman Scattering Enhancement by Optical Confinement in a Semiconductor Planar Microcavity. *Phys. Rev. Lett.* **75**, 3764–3767 (1995).

15. Fainstein, A., Jusserand, B. & Thierry-Mieg, V. Cavity-Polariton Mediated Resonant Raman Scattering. *Phys. Rev. Lett.* **78**, 1576–1579 (1997).
16. Khajavikhan, M. *et al.* Thresholdless nanoscale coaxial lasers. *Nature* **482**, 204–207 (2012).
17. Wu, K., Park, Y.-S., Lim, J. & Klimov, V. I. Towards zero-threshold optical gain using charged semiconductor quantum dots. *Nature Nanotech* **12**, 1140–1147 (2017).
18. Jagsch, S. T. *et al.* A quantum optical study of thresholdless lasing features in high- $\beta$  nitride nanobeam cavities. *Nat Commun* **9**, 564 (2018).
19. Rüter, C. E. *et al.* Observation of parity–time symmetry in optics. *Nature Phys* **6**, 192–195 (2010).
20. Peng, B. *et al.* Parity–time-symmetric whispering-gallery microcavities. *Nature Phys* **10**, 394–398 (2014).
21. Chang, L. *et al.* Parity–time symmetry and variable optical isolation in active–passive-coupled microresonators. *Nature Photon* **8**, 524–529 (2014).
22. Gao, T. *et al.* Observation of non-Hermitian degeneracies in a chaotic exciton-polariton billiard. *Nature* **526**, 554–558 (2015).
23. Yuen-Zhou, J. *et al.* Plexciton Dirac points and topological modes. *Nat Commun* **7**, 11783 (2016).
24. Richter, S. *et al.* Exceptional points in anisotropic planar microcavities. *Phys. Rev. A* **95**, 023836 (2017).
25. Gao, T. *et al.* Chiral Modes at Exceptional Points in Exciton-Polariton Quantum Fluids. *Phys. Rev. Lett.* **120**, 065301 (2018).
26. Gao, W., Li, X., Bamba, M. & Kono, J. Continuous transition between weak and ultrastrong coupling through exceptional points in carbon nanotube microcavity exciton–polaritons. *Nature Photonics* **12**, 362–367 (2018).
27. Zhang, J. *et al.* A phonon laser operating at an exceptional point. *Nature Photon* **12**, 479–484 (2018).
28. Kremer, M. *et al.* Demonstration of a two-dimensional  $\mathcal{PT}$ -symmetric crystal. *Nat Commun* **10**, 435 (2019).

29. Khurgin, J. B. Exceptional points in polaritonic cavities and subthreshold Fabry–Perot lasers. *Optica*, **OPTICA 7**, 1015–1023 (2020).
30. Song, H. G., Choi, M., Woo, K. Y., Park, C. H. & Cho, Y.-H. Room-temperature polaritonic non-Hermitian system with single microcavity. *Nat. Photon.* **15**, 582–587 (2021).
31. Su, R. *et al.* Direct measurement of a non-Hermitian topological invariant in a hybrid light-matter system. *Science Advances* **7**, eabj8905 (2021).
32. Feng, L., Wong, Z. J., Ma, R.-M., Wang, Y. & Zhang, X. Single-mode laser by parity-time symmetry breaking. *Science* **346**, 972–975 (2014).
33. Hodaei, H., Miri, M.-A., Heinrich, M., Christodoulides, D. N. & Khajavikhan, M. Parity-time-symmetric microring lasers. *Science* **346**, 975–978 (2014).
34. Peng, B. *et al.* Loss-induced suppression and revival of lasing. *Science* **346**, 328–332 (2014).
35. Jing, H. *et al.* PT -Symmetric Phonon Laser. *Phys. Rev. Lett.* **113**, 053604 (2014).
36. Özdemir, Ş. K., Rotter, S., Nori, F. & Yang, L. Parity–time symmetry and exceptional points in photonics. *Nat. Mater.* **18**, 783–798 (2019).
37. Miri, M.-A. & Alù, A. Exceptional points in optics and photonics. *Science* **363**, eaar7709 (2019).
38. Feng, L., El-Ganainy, R. & Ge, L. Non-Hermitian photonics based on parity–time symmetry. *Nature Photon* **11**, 752–762 (2017).
39. El-Ganainy, R. *et al.* Non-Hermitian physics and PT symmetry. *Nature Phys* **14**, 11–19 (2018).
40. Kepesidis, K. V. *et al.* -symmetry breaking in the steady state of microscopic gain–loss systems. *New J. Phys.* **18**, 095003 (2016).
41. Wang, G. *et al.* *Colloquium* : Excitons in atomically thin transition metal dichalcogenides. *Rev. Mod. Phys.* **90**, 021001 (2018).
42. Ye, Y. *et al.* Monolayer excitonic laser. *Nature Photon* **9**, 733–737 (2015).
43. Shang, J. *et al.* Room-temperature 2D semiconductor activated vertical-cavity surface-emitting lasers. *Nat Commun* **8**, 543 (2017).

44. Liu, X. *et al.* Strong light–matter coupling in two-dimensional atomic crystals. *Nature Photon* **9**, 30–34 (2015).
45. Dhara, S. *et al.* Anomalous dispersion of microcavity trion-polaritons. *Nature Phys* **14**, 130–133 (2018).
46. Aslan, O. B., Chenet, D. A., van der Zande, A. M., Hone, J. C. & Heinz, T. F. Linearly Polarized Excitons in Single- and Few-Layer ReS<sub>2</sub> Crystals. *ACS Photonics* **3**, 96–101 (2016).
47. Dhara, A. *et al.* Additional excitonic features and momentum-dark states in ReS<sub>2</sub>. *Phys. Rev. B* **102**, 161404 (2020).
48. Chakrabarty, D. *et al.* Interfacial anisotropic exciton-polariton manifolds in ReS<sub>2</sub>. *Optica, OPTICA* **8**, 1488–1494 (2021).
49. McCreary, A. *et al.* Intricate Resonant Raman Response in Anisotropic ReS<sub>2</sub>. *Nano Lett.* **17**, 5897–5907 (2017).
50. Jadczyk, J. *et al.* Exciton binding energy and hydrogenic Rydberg series in layered ReS<sub>2</sub>. *Sci Rep* **9**, 1578 (2019).

## Methods:

### Sample fabrication

We prepared three samples of ReS<sub>2</sub> with the same thickness: two embedded in a microcavity and the other stacked on SiO<sub>2</sub>/Si (henceforth also referred to as a 'bare' sample). The microcavity consists of two distributed Bragg reflectors (DBRs). The bottom mirror comprises 9.5 pairs of SiO<sub>2</sub>/Ta<sub>2</sub>O<sub>5</sub> films, grown using the RF sputtering technique. A ReS<sub>2</sub> crystal of thickness 10 nm is exfoliated by the dry transfer method and transferred on the bottom mirror. The top DBR of 7.5 pairs of SiO<sub>2</sub>/Ta<sub>2</sub>O<sub>5</sub> is then deposited using the same sputtering method. The other sample is prepared by dry transfer of exfoliated 10 nm thick ReS<sub>2</sub> crystal on the Si/SiO<sub>2</sub> substrate. We estimate the sample thickness from the optical image. Sample image is shown in the Extended Data Fig. 4.

### Measurement

All optical measurements were performed with the sample placed in a closed cycle microscopy cryostat (Montana Instruments) with a variable temperature range of 3.2 to 295 K. For the Raman study, we excite the sample from the top with a Ti: Sapphire laser (Coherent—MIRA) in the quasi-CW mode with the pump energy of 1.564 eV ( $\lambda_{excitation} = 792.8\text{ nm}$ ). The excitation path contains a linear polarizer followed by a half-wave plate mounted on a motorized rotational stage to control the polarization of the pump beam. Polarization state of light beam was preserved throughout the optical path via a special design in our optical setup as discussed elsewhere<sup>51</sup> for polarization resolved Raman spectroscopy. The laser beam was focused with the spot size  $\sim 1\ \mu\text{m}$  by a 60X objective lens with a numerical aperture of 0.7 N.A. The Raman Stokes signal is collected through the same objective lens and dispersed by a diffraction grating with 1200 grooves per mm and detected by a nitrogen-cooled CCD (Pylon 400) with spectral resolution of  $0.5\text{ cm}^{-1}$ . In the temperature dependent power variation study, to attenuate scattered light of the laser from the optical elements in the beam path and increase the signal-to-noise ratio, an analyzer is kept before the spectrometer, crossed with the laser polarization. A broadband light source (Thorlabs SLS202L) is used for reflectance measurements.

### Stacking order in ReS<sub>2</sub>

We identify several Raman modes which exactly match with existing literature<sup>49,52</sup>, such as:  $A_g^4$  ( $139\text{ cm}^{-1}$ ),  $A_g^5$  ( $144\text{ cm}^{-1}$ ),  $A_g^1$  ( $152\text{ cm}^{-1}$ ),  $A_g^7$  ( $214\text{ cm}^{-1}$ ),  $A_g^8$  ( $236\text{ cm}^{-1}$ ),  $A_g^9$  ( $276\text{ cm}^{-1}$ ),  $A_g^{10}$  ( $284\text{ cm}^{-1}$ ),  $A_g^{12}$  ( $311\text{ cm}^{-1}$ ),  $A_g^{13}$  ( $320\text{ cm}^{-1}$ ),  $A_g^{14}$  ( $325\text{ cm}^{-1}$ ),  $A_g^{15}$  ( $349\text{ cm}^{-1}$ ),  $A_g^{16}$  ( $369\text{ cm}^{-1}$ ),  $A_g^{17}$  ( $378\text{ cm}^{-1}$ ),  $A_g^{18}$  ( $408\text{ cm}^{-1}$ ),  $A_g^3$  ( $420\text{ cm}^{-1}$ ) and  $A_g^2$  ( $440\text{ cm}^{-1}$ ), shown in the Extended Data Fig. 5.

Recently, it has been reported that ReS<sub>2</sub> crystal has two stable stacking orders (AA and AB)<sup>52</sup>, which have been identified by the separation between the  $A_g^4$  and  $A_g^1$  modes. The separation between these two modes in both cases (inside microcavity and bare sample) is  $13\text{ cm}^{-1}$ , as found in AA stacking ReS<sub>2</sub> crystal, as shown in Extended Data Fig. 1.

### Model for Non-Hermitian PT-Symmetric system

The eigenvalues of the matrix from Eqn. (1) are:

$$E^\pm = \epsilon + i(\delta_1 - \delta_2)/2 \pm \sqrt{g^2 - \left(\frac{\delta_1 + \delta_2}{2}\right)^2} \dots\dots\dots (3)$$

In the case of finite threshold lasing (pumping along  $d_2$  polarization), we observe one lasing mode (polarized along  $d_1$ ) and one non-lasing mode (polarized along  $d_2$ ) at the same energy ( $\epsilon$ ). Thus, the two eigenvalues  $E^\pm$  must satisfy the following conditions: (i) real part should be the same ( $\epsilon$ ), and (ii) imaginary part should be opposite in sign, positive sign implying lasing mode and negative sign lossy mode. Condition (i) is satisfied in the regime,  $g \leq \delta$ , where  $\delta = \frac{(\delta_1 + \delta_2)}{2}$ . Since the quantity  $\sqrt{g^2 - \left(\frac{\delta_1 + \delta_2}{2}\right)^2}$  is always smaller than  $\frac{(\delta_1 - \delta_2)}{2}$ , condition (ii) is only possible when  $\frac{(\delta_1 - \delta_2)}{2} = 0$ , which implies  $\delta_1 = \delta_2$ . Thus, from our arguments, based on pure experimental observations, we find the Hamiltonian  $H$  is PT-symmetric, since the diagonal elements are complex conjugates:

$$H = \begin{pmatrix} \epsilon + i\delta & g \\ g & \epsilon - i\delta \end{pmatrix}$$

The mode  $E^+$  with a positive imaginary part is responsible for finite threshold mode, and  $E^-$  non-lasing lossy mode of the cavity. For excitation polarization along  $d_2$ , a large amplitude of  $|\psi_2\rangle$  lies in the stop band of the cavity, leading to a weak coupling ( $g < \delta$ ) condition and hence finite threshold lasing in PT broken phase.

On the other hand, ZTPRL is obtained when only a single mode exists inside the cavity, or the eigen modes coalesce. This happens in the case when  $g = \delta$ . In this condition, the eigenvalues are real and degenerate, and the system is in PT-symmetric phase. Our experimental observations suggest that the coupling strength  $g$  should depend on the pump polarization, which can be understood as follows: When excited along  $d_1$  polarization, a large amplitude of  $|\psi_1\rangle$  being amplified as it is supported by  $L_1$  causing the enhancement in  $g$  reaches its maximum  $g = \delta$ , showing zero-threshold lasing. Interestingly, we observe only the  $A_g^7$  mode which coincides exactly at the dip of the  $L_1$  band shows ZTPRL irrespective of the polarization of the pump beam.

### Rate equation model for zero and finite threshold PT- symmetric polariton Raman laser

The power dependent intensity of polariton Raman laser in the zero and finite threshold regime can be understood from the rate equation model<sup>53-56</sup> we describe below.

The polariton is pumped to a virtual state  $|\psi(\epsilon_{EP}, k_{EP})\rangle$  at the EP of bands  $U_1$  and  $L_2$ , with generation rate  $P_{int}$ . Through free-space spontaneous Raman scattering (with rate  $S$ ), the excited polaritons are instantaneously scattered into the degenerate ground states  $|\psi_1(\epsilon, k_{EP})\rangle$ ,  $|\psi_2(\epsilon, k_{EP})\rangle$ , having the same momentum but different polarizations as shown in Extended Data Fig. 6. Stokes shifted PR modes are thus emitted along  $d_1$  and  $d_2$  directions. The PR modes along  $d_1$  direction is confined in the cavity via the  $L_1$  polariton branch, which enhances the Raman scattering rate ( $S$ ) by the Purcell factor ( $F$ ), creating the lasing mode with energy  $E^+$ . On the other hand, PR modes along  $d_2$  direction fall in the stopband and are not confined, forming the lossy mode with

energy  $E^-$ . The spontaneous emission rate from lasing and lossy mode is  $\beta SF$  and  $(1 - \beta)S$  respectively. Additionally, stimulated emission rate from lasing mode is  $\beta SF N_p$ , where  $N_p$  is the number of photons associated with PR mode in the cavity, with a decay rate  $\gamma_c$ .

The rate equations can be written as,

$$\frac{d}{dt} \begin{pmatrix} N_R \\ N_p \end{pmatrix} = \begin{pmatrix} -\beta SF - (1 - \beta)S & -\beta SF N_R \\ \beta SF(1 + N_p) & -\gamma_c \end{pmatrix} \begin{pmatrix} N_R \\ N_p \end{pmatrix} + \begin{pmatrix} P_{int} \\ 0 \end{pmatrix}$$

Here,  $N_R$  is the number of molecules in the virtual state.

The equation (2) can be written as,

$$I_{out} = \frac{1}{2} c_2 \left( c_1 P_{int} + \beta - 1 - \beta F + \sqrt{(\beta - 1 - c_1 P_{int} + \beta F)^2 + 4\beta F c_1 P_{int}} \right) \dots \dots \dots (4)$$

Where  $c_1$  and  $c_1$  are scaling parameters.

$c_1$  to scale the measured input power to the real input power.

$c_2$  to scale the measured intensity by the spectrometer to output power, which depends on the spectrometer gain and exposure time as well as collection optics efficiency.

To fit the saturation behavior at higher power equation (4) can be modified as,

$$I_{out} = \frac{1}{2} c_2 \left( c_1 P_{int} + \beta - 1 - \beta F + \sqrt{(\beta - 1 - c_1 P_{int} + \beta F)^2 + 4\beta F c_1 P_{int}} \right) - c_3 c_1 P_{int}^{1.5} \dots \dots (5)$$

Where  $c_3$  is the fitting parameter to capture the 3<sup>rd</sup> order non-linear loss.

All the fitted parameters are listed in the Extended Data Table 1 and 2.

## References:

51. Pattanayak, A. K. *et al.* A Steady-State Approach for Studying Valley Relaxation Using an Optical Vortex Beam. *Nano Lett.* **22**, 4712–4717 (2022).
52. Zhou, Y. *et al.* Stacking-Order-Driven Optical Properties and Carrier Dynamics in ReS<sub>2</sub>. *Adv. Mater.* **32**, 1908311 (2020).
53. Yokoyama, H. & Brorson, S. D. Rate equation analysis of microcavity lasers. *Journal of Applied Physics* **66**, 4801–4805 (1989).
54. Bjork, G. & Yamamoto, Y. Analysis of semiconductor microcavity lasers using rate equations. *IEEE J. Quantum Electron.* **27**, 2386–2396 (1991).
55. *Microcavities*. (Oxford Univ. Press, 2011).
56. Khurgin, J. B. & Noginov, M. A. How Do the Purcell Factor, the Q-Factor, and the Beta Factor Affect the Laser Threshold? *Laser & Photonics Reviews* **15**, 2000250 (2021).

**Extended Data Table 1** | Fitted parameter for different excitation polarization of the  $A_g^{12}$  mode

Calculated Purcell factor (F) ~ 40.

**Fitted parameters without loss**

	F from fitting	$\beta$	$c_1$	$c_2$
Excitation polarization along $d_1$ axis	39	1	21	447
Excitation polarization along $d_2$ axis	30	0.01	0.22	34234

**Fitted parameters with loss (WL)**

	F from fitting	$\beta$	$c_1$	$c_2$	$c_3$
Excitation polarization along $d_1$ axis	35	1	28	481	105
Excitation polarization along $d_2$ axis	40	0.01	0.77	14507	8256

**Extended Data Table 2** | Fitted parameter for fixed excitation polarization  $d_2$  and different temperature of the  $A_{7g}$  mode

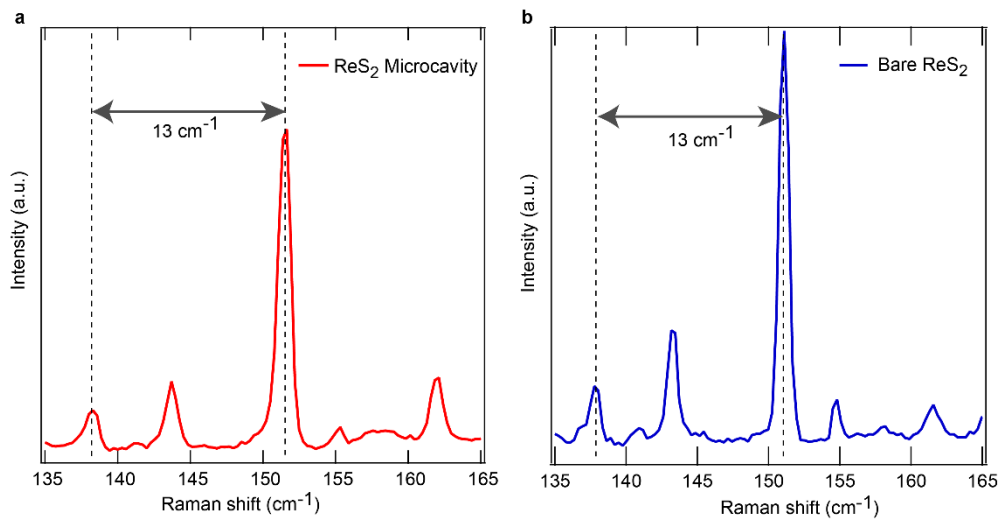
**Fitting parameter without loss**

Temperature	F from fitting	$\beta$	$c_1$	$c_2$
4 K	80	1	46	217
150 K	35	0.007	0.36	6251
200 K	20	0.004	0.16	20934
RT	3	0.001	0.07	422058

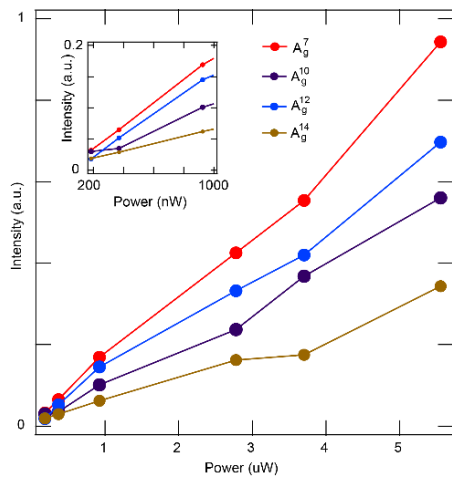
**Fitting parameter with loss (WL)**

Temperature	F from fitting	$\beta$	$c_1$	$c_2$	$c_3$
4 K	80	1	0.01	1006480	322710
150 K	36	0.007	0.4	14222	11027

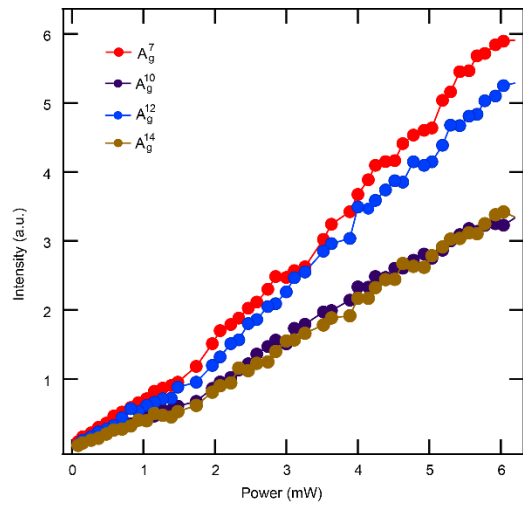
200 K	24	0.004	0.15	48547	11908
-------	----	-------	------	-------	-------



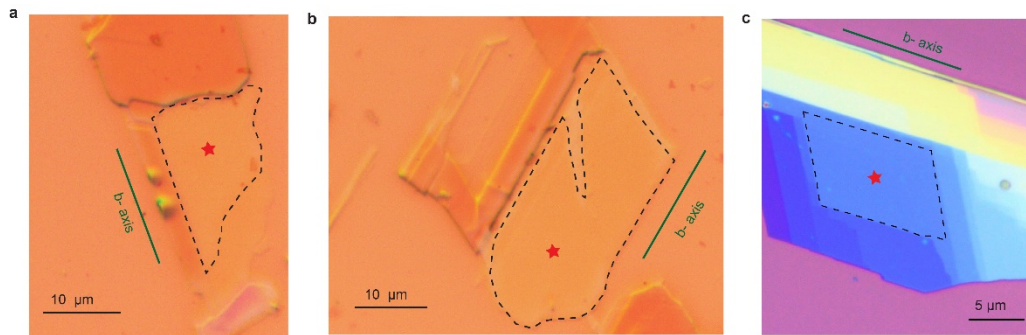
**Extended Data Fig. 1 | Stacking order dependent Raman modes in ReS<sub>2</sub>.** The  $A_g^4$  and  $A_g^1$  Raman modes exhibit a separation of  $13 \text{ cm}^{-1}$  indicating AA stacking in both scenarios: (a) ReS<sub>2</sub> within the microcavity and (b) ReS<sub>2</sub> on SiO<sub>2</sub>/Si



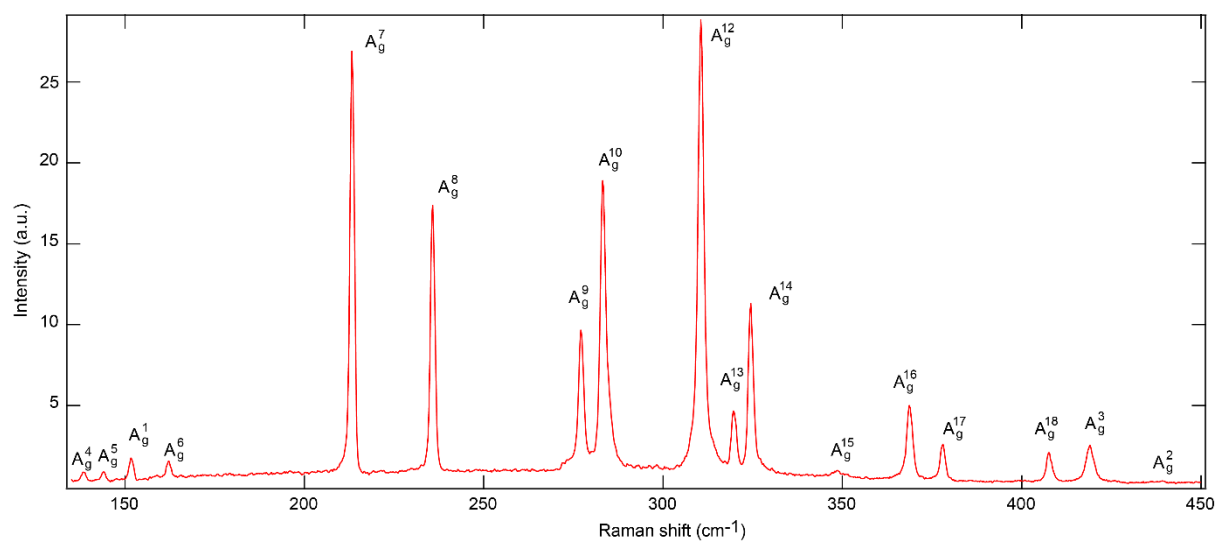
**Extended Data Fig. 2** | Threshold scan in hundreds of nW range for the case of zero threshold lasing when pump beam polarization is along  $d_1$ .



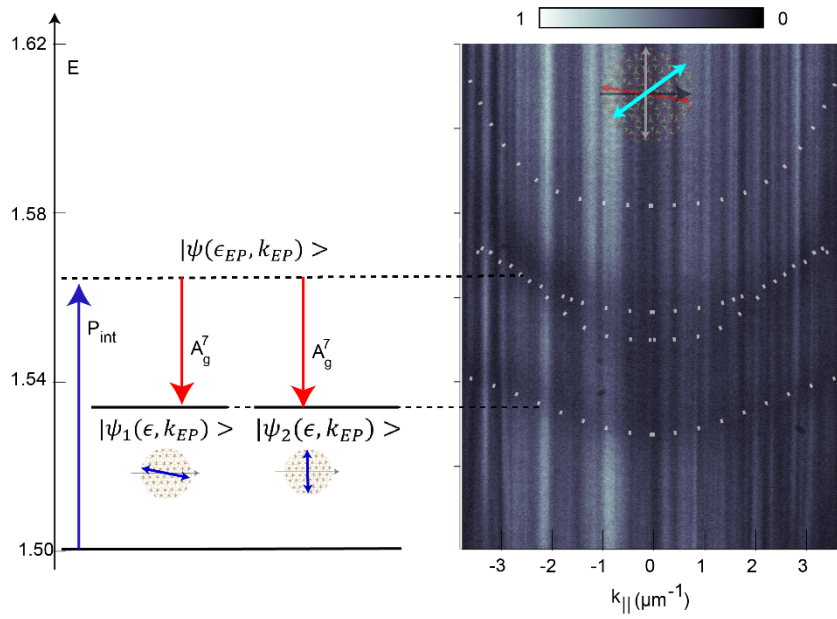
**Extended Data Fig. 3** | Input power dependence with excitation polarization along  $d_2$  and detection along  $d_2$ .



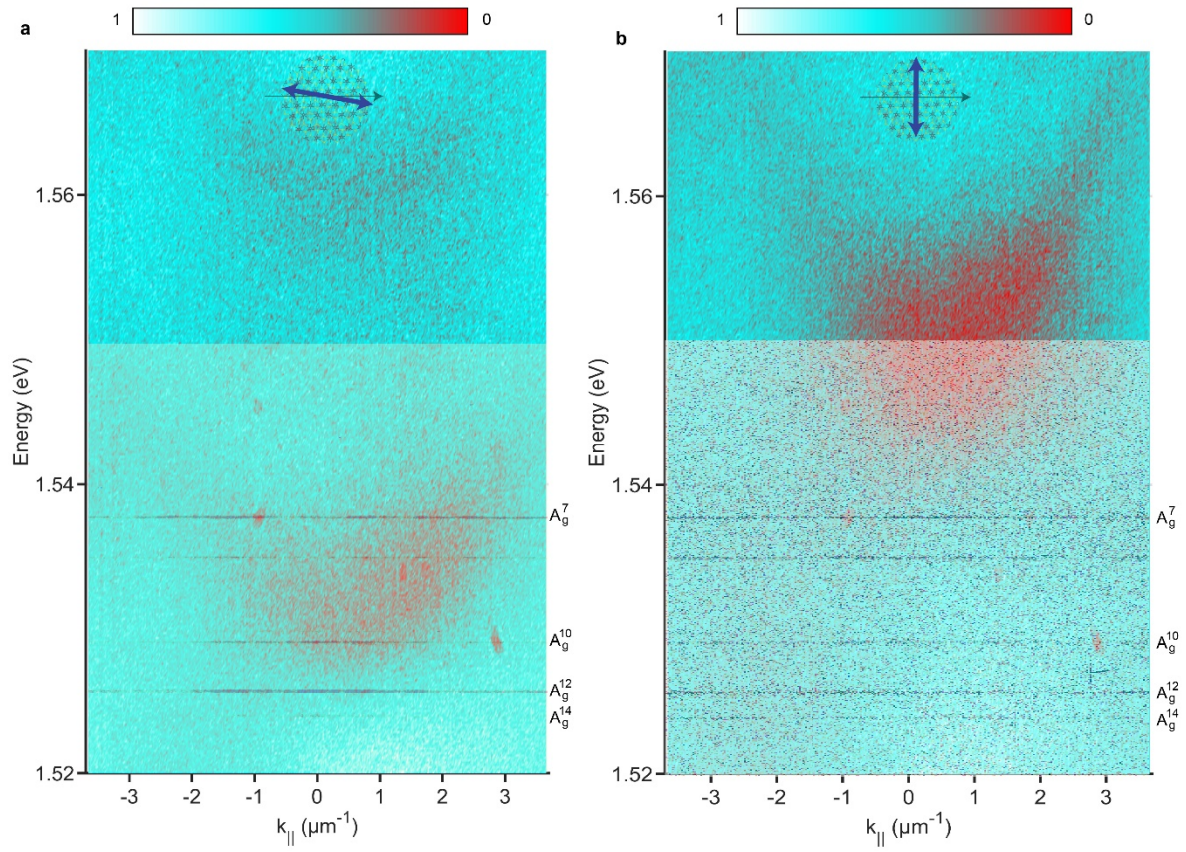
**Extended Data Fig. 4 | Optical microscope images of (a) ReS<sub>2</sub> inside microcavity. All data presented in Figs. 1-4 in the article correspond to experiments done on this sample. (b) Different ReS<sub>2</sub> sample inside microcavity with same thickness as (a) whose corresponding experimental data is shown in Extended Data Fig 8. (c) Bare ReS<sub>2</sub> (ReS<sub>2</sub> on SiO<sub>2</sub>/Si). The black dotted lines indicate the boundary of the sample section that is 10 nm in thickness. The red starting point denotes the excitation point.**



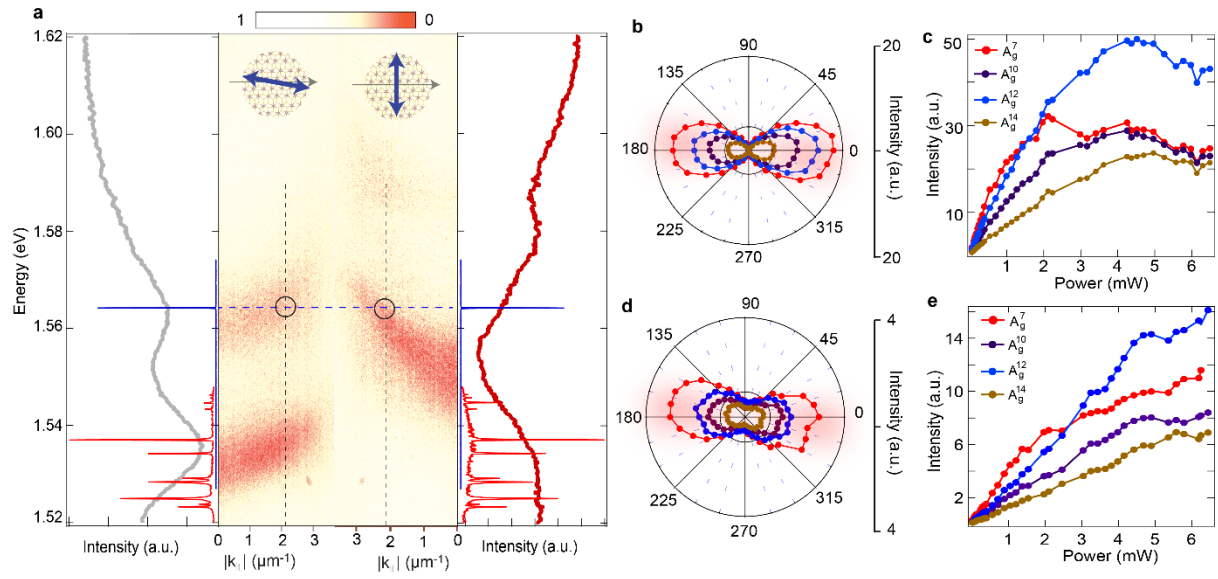
**Extended Data Fig. 5** | Stokes Raman spectra measured for ReS<sub>2</sub> inside microcavity, with the distinct modes labelled.



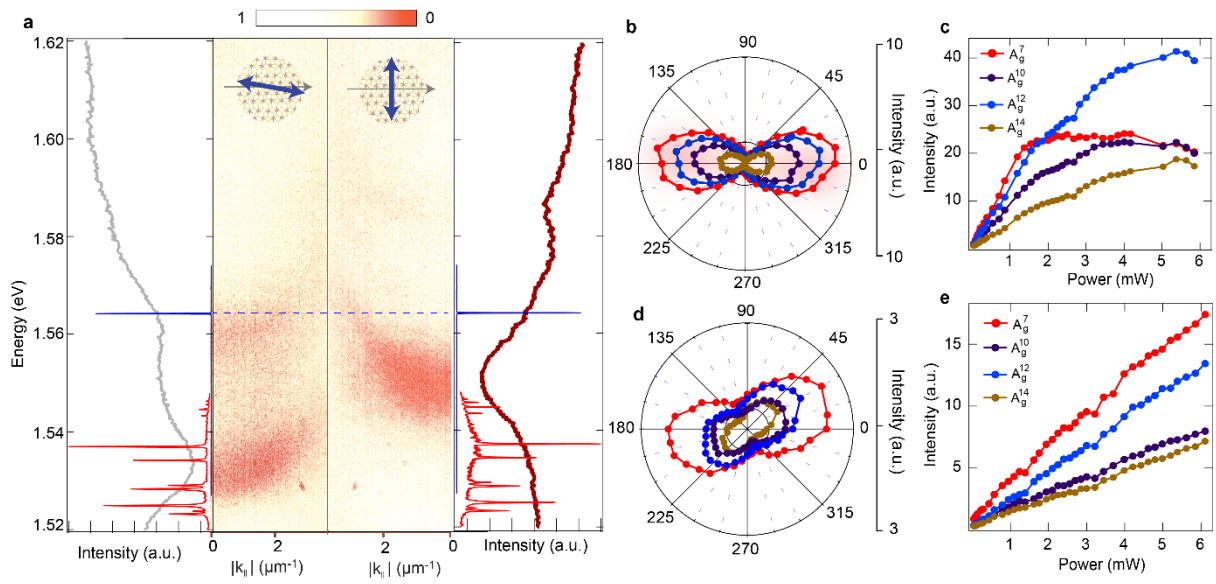
**Extended Data Fig. 6** | Rate equation model schematic for ZTPRL showing the states involved in stimulated Raman scattering. (Right) Experimental angle-resolved reflectance taken for an intermediate probe polarization, showing two anisotropic polariton modes corresponding to different polarizations coalescing at the EP near the excitation energy.



**Extended Data Fig. 7 | Directionality of the lasing emission from the PR modes** (a) The angle-resolved Raman spectra plots display the PR modes profiles, superimposed with the polariton branches from the angle-resolved reflectance spectra. The figure highlights the  $A_g^7$ ,  $A_g^{10}$ ,  $A_g^{12}$  and  $A_g^{14}$  modes, which exhibit lasing emission and fulfil the momentum matching condition. (b) Those same RP modes do not lase along the  $d_2$  axis do not display any emission pattern.



**Extended Data Fig. 8 | Experimental results for alternative sample shown in extended data fig 4 b.** (a) Angle resolved reflectance for probe beam polarization along  $d_1$  (right) and  $d_2$  (left) axis. EP regions in polariton dispersion for this sample are marked (black circles). Adjacent plots along the extreme left and extreme right show corresponding integrated reflectance, and the RP modes (red) when the pump beam (blue) is polarized along those directions. (b) Polar plot of emission intensity as a function of analyser angle for the pump beam polarization along  $d_1$ , showing a strongly polarized emission. (c) Power dependence data for excitation along  $d_1$  showing ZTPRL for all the PR modes. (d) A similar polar plot as figure (b) with the pump polarization beam along  $d_2$ . (e) The power dependence plot showing the finite threshold lasing behavior with a kink near 2 mW for  $A_g^{10}$ ,  $A_g^{12}$  and  $A_g^{14}$  with pump polarization along  $d_2$ .



**Extended Data Fig. 9 | Experimental results after rotating sample by 45 degrees (orientation with no EPs)**  
 (a) Angle resolved reflectance for the probe beam polarization along  $d_1$  (right) and  $d_2$  (left) axis. No EPs are found for this orientation. (b) Polar plot of emission intensity as a function of analyser angle for the pump beam polarization is along  $d_1$  showing a strong polarized emission. (c) Power dependence data for excitation along  $d_1$  showing ZTPRL for all the PR modes. (d) A similar polar plot as figure (b) with the pump polarization beam along  $d_2$ . Here all the modes are polarized along the different directions indicating there is no lasing happening for any mode. (e) The power dependence plot showing linear behavior of the PR modes with no lasing threshold for pump polarization along  $d_2$ .